Excited state dynamics and time-resolved photoelectron spectroscopy of *para – xylylene*

Kevin Issler, Anja Röder, Florian Hirsch, Lionel Poisson, Ingo Fischer, Roland Mitrić, Jens Petersen

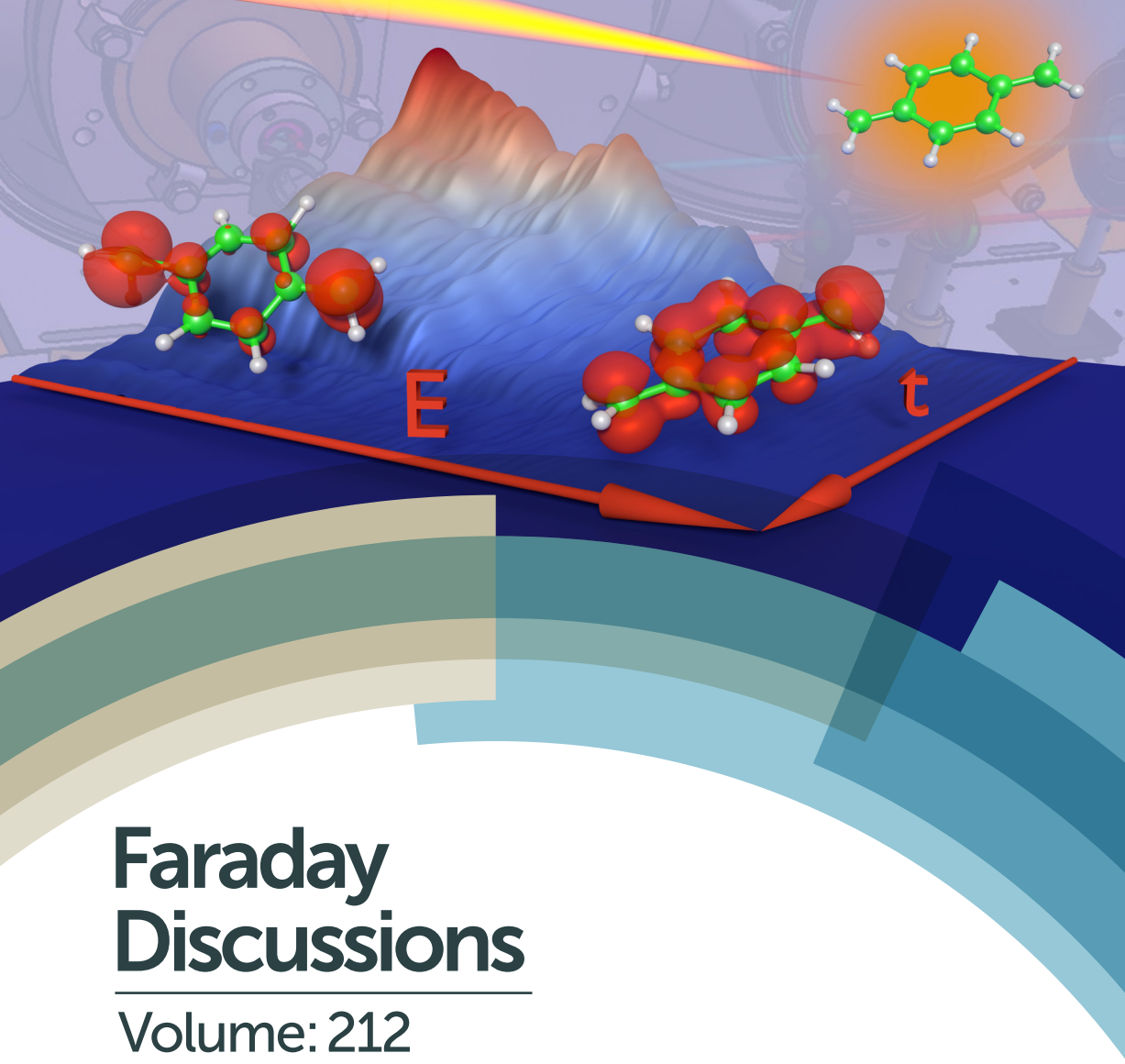

Faraday Discussions

Volume: 212

Quantum Effects in Small Molecular Systems

ROYAL SOCIETY OF CHEMISTRY

Faraday Discussions

Cite this: *Faraday Discuss.*, 2018, **212**, 83

PAPER

Excited state dynamics and time-resolved photoelectron spectroscopy of *para*-xylylene†

Kevin Issler,‡[a] Anja Röder,‡§[ab] Florian Hirsch,[a] Lionel Poisson,*[b] Ingo Fischer,*[a] Roland Mitrić*[a] and Jens Petersen*[a]

Received 24th April 2018, Accepted 8th May 2018
DOI: 10.1039/c8fd00083b

We investigated the excited-state dynamics of *para*-xylylene using a combination of field-induced surface hopping (FISH) simulations and time-resolved ionisation experiments. Our simulations predict an ultrafast decay of the initially excited bright state (S_2/S_3) to the S_1 state on a sub-100 fs time scale, followed by return to the ground state within ~1 ps. This is accompanied by a transient change of the biradical character of the molecule, as monitored by calculating natural orbital occupation numbers. Specifically, the initially low biradicality is increased by electronic excitation as well as by vibrational activation. Experimentally, *para*-xylylene was generated by pyrolysis from [2,2]paracyclophane and excited with 266 nm radiation into the S_2/S_3 bright state. The subsequent dynamics were followed using ionisation as the probe step, with both mass spectra and photoelectron spectra recorded as a function of pump–probe delay. The observed decay of photoelectron and photoion intensities closely matches the theoretical predictions and is consistent with the sequential mechanism found in the simulations. This mechanism exhibits characteristic signatures in both time-resolved mass and photoelectron spectra, in particular in the appearance of fragment ions that are exclusively generated from the S_1 state. This allows for a separation of the S_2 and S_1 dynamics in the photoelectron and mass spectra. An excellent agreement between the observed and the simulated ion signal is observed.

1 Introduction

Combustion and pyrolysis of aromatic molecules often proceed *via* radical intermediates formed by H atom abstraction, a simple example being the

[a]*Institute of Physical and Theoretical Chemistry, University of Würzburg, Am Hubland, D-97074 Würzburg, Germany. E-mail: ingo.fischer@uni-wuerzburg.de; roland.mitric@uni-wuerzburg.de; jens.petersen@uni-wuerzburg.de*

[b]*LIDYL, CEA, CNRS, Université Paris-Saclay, CEA Saclay, 91191 Gif-sur-Yvette, France. E-mail: lionel.poisson@cea.fr*

† Electronic supplementary information (ESI) available. See DOI: 10.1039/c8fd00083b

‡ These authors contributed equally to this work.

§ Present address: Department of Chemistry, University of Ottawa, 10 Marie Curie, Ottawa, Ontario K1N 6N5, Canada.

generation of benzyl radicals from toluene.[1–4] If a second methyl group is added to the toluene structure, the family of xylene molecules is obtained, with the three isomers *ortho*-, *para*- and *meta*-xylene differing by the relative position of the two methyl groups. Xylenes are frequently found in commercial fuels, often added on purpose due to their anti-knocking properties.[5] If the pyrolysis of xylenes proceeds in a way similar to toluene, this should result in hydrogen abstraction from both of the two methyl groups, leading to intermediates that formally possess two radical centres and hence could be qualified as biradicals. Early studies of Szwarc[1] have indeed shown that the first step in the pyrolysis of xylenes is the abstraction of a single hydrogen atom, leading to the formation of resonantly stabilised xylyl radicals. The observed reaction products for *meta*- and *ortho*-xylene, specifically the formation of a dibenzyl derivative for *meta*-xylene, provide strong evidence that only mono-radicals are involved in the pyrolysis mechanism. By contrast, the pyrolysis of *para*-xylene results in the formation of a solid polymer, which is formed from half of the involved molecules. As an explanation, the disproportionation of the initially formed *para*-xylyl radicals was proposed, leading to *para*-xylene molecules and *para*-xylylene biradicals. By condensation on cooled tube walls, the latter are converted into the above-mentioned polymer. The transient presence of *para*-xylylene in the gas phase was evidenced by the formation of its diiodide in the presence of iodine vapour.[6] Later studies provided a more detailed understanding of the reactions and resulting products involved in *para*-xylene pyrolysis,[7,8] among them its cyclic dimer, [2,2]paracyclophane.[7] The latter is a stable, commercially available solid and has been used as an alternative precursor of *para*-xylylene and its polymer.[9] By employing substituted *para*-xylylene subunits, a whole class of poly-*para*-xylylenes is accessible, bearing substituents such as halogens, or methyl and ethyl groups. These polymers exhibit remarkable physical properties, being only very weakly permeable for permanent gases such as H_2, O_2 or N_2 as well as being highly electrically insulating.[9] Together with their ability to be deposited on surfaces in thin films, this has enabled their technical use for insulating coatings. In this context, the polymers are commercially known as parylenes. Novel routes to oligomer formation in solution have in recent times also allowed to follow the detailed reaction mechanism by means of NMR spectroscopy.[10] Besides the aforementioned thermal pathways leading to *para*-xylylene, its formation can also be induced photochemically by UV irradiation of *para*-xylyl radicals.[11]

The electronic structure of *para*-xylylene in its ground state has been the subject of several experimental and theoretical investigations in recent decades. A simple valence bond picture gives rise to the resonance structures shown on the right in Fig. 1, one of which is quinoidal and should exhibit at least two distinct carbon–carbon bond lengths, while the other is of biradical character with a benzenoid ring system, for which equal bond lengths are expected. It has been found quite early that the quinoidal structure clearly dominates over the biradical one,[7,12] which is in contrast to, *e.g.*, the *meta* isomer of xylylene[13,14] and makes *para*-xylylene essentially a closed-shell system. This conclusion has been supported by a number of experimental studies: NMR spectroscopy shows the expected chemical shifts for a quinone structure, and no ESR signal indicating unpaired electrons was observed.[15] The UV and IR spectra in the solid phase are in agreement with theoretically predicted spectra based on the quinone structure,[16] with the UV spectrum exhibiting a broad absorption band centred around

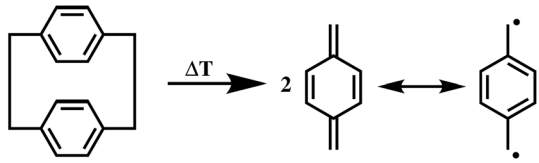

Fig. 1 Reaction scheme for the generation of *para*-xylylene from the pyrolysis of [2.2] paracyclophane. On the product side, both the quinoid (left) as well as the benzenoid (right) resonance structures are shown.

300 nm.[16] Two different C–C bond distances, corresponding to double and single bonds, were found in electron diffraction experiments,[17] which is again consistent with a quinoidal closed-shell structure. Computational studies have provided further support. Employing a configuration interaction approach including single and double excitations (CISD) with perturbatively selected configurations and using a double zeta Gaussian basis set, Ha[18] predicted the biradical triplet state to lie 2.27 eV above the closed-shell ground state, while more recent investigations using *ab initio* multi-configurational perturbation theory (CASSCF/MRMP2) predicted a value of 1.65 eV.[19] Attempts to calculate excited electronic states have been made as well. Flynn and Michl employed a semiempirical PPP (Pariser–Parr–Pople) model to determine the lowest states of $\pi\pi^*$ character.[13] They showed that the lowest lying excited singlet state should be doubly excited, while the first symmetry-allowed singly excited state is expected at somewhat higher energies. In his *ab initio* CISD study,[18] Ha calculated several singlet and triplet excited states of $\pi\pi^*$ and $\pi\sigma^*$ character, obtaining a singly excited $^1B_{2u}$ $\pi\pi^*$ state at 4.55 eV as the lowest lying one.[20] However, due to the restricted selection of reference configurations and the basis set containing neither polarisation nor diffuse functions, the energy and character of electronic states found in this study have to be considered with caution. In particular, the doubly excited $\pi\pi^*$ state proposed by Flynn and Michl seems to appear far too high in energy (6.39 eV), and the lack of diffuse basis functions leads to the complete absence of Rydberg states, which should appear well below 6 eV, as will be discussed in the present contribution. The CASSCF/MRMP2 study of Bobrowski *et al.* restricts itself to the lowest open-shell singlet state, which is found as a $^1B_{2u}$ ($\pi\pi^*$) state at 4.31 eV.[19,20]

The first experimental determination of the ionisation energies of *para*-xylylene was performed using He(I) photoelectron spectroscopy,[21] with a first ionisation energy of ~7.87 eV and a second one of 9.7 eV. Recently, the first ionisation energy was measured more accurately by threshold photoelectron spectroscopy,[22] providing a value of 7.85 eV for the vibronic 0–0 transition. The semiempirical MNDO calculations of Dewar match these values reasonably well, providing 8.18 and 9.94 eV for the lowest two ionisation energies.[23] The aforementioned study of Ha led to values of 7.12 and 9.27 eV,[18] clearly underestimating the experimental results.

Despite its importance in organic synthesis and combustion chemistry, and the considerable amount of previous work on the electronic structure, the photodynamics of *para*-xylylene has remained unexplored so far. The present contribution aims at closing this gap by a combination of nonadiabatic molecular dynamics simulations with femtosecond time-resolved time-of-flight mass

spectrometry (fs-TOF-MS) and photoelectron spectroscopy (fs-TRPES). This will provide information about the energetics and time scales of the relaxation of the involved electronic states and the radiationless deactivation processes following initial photoexcitation at 266 nm. The combination of experiment and theory makes it possible to establish a direct connection between the experimental time-resolved observables and the underlying molecular mechanisms. This approach has been employed before to elucidate the dynamics of other reactive molecules,[24–31] although not yet on a molecule with (partial) biradical character.

2 Experimental methods

The experimental setup has been described previously.[25] In brief, *para*-xylylene was produced *via* flash pyrolysis[32] from [2.2]paracyclophane (see Fig. 1). The precursor was placed in an oven operated at 115 °C, right before a water-cooled solenoid pulsed valve operating at 20 Hz, and seeded into helium at 2.5 bar absolute pressure. [2.2]Paracyclophane was purchased from Sigma-Aldrich and used without further purification. After pyrolysis, the *para*-xylylene–helium mixture was expanded as a free jet into the sample chamber kept at pressures around 5×10^{-5} mbar, and passed a 1 mm skimmer 2 cm downstream of the pyrolysis tube into the detection chamber (4×10^{-7} mbar). The latter was equipped with a time-of-flight mass detector (TOF-MS) and a velocity-map-imaging detector (VMI) orthogonal to the molecular jet to record the time-resolved photoelectron spectra (TRPES).[33]

The LUCA/SLIC laser facility provided the Ti:Sa oscillator amplifier laser system used for the pump–probe experiments as described previously.[34] The tripled fundamental of the Ti:Sa laser (266 nm, 8 μJ) was used as the pump pulse, for the probe pulse either the fundamental of the Ti:Sa laser (794 nm, 1.0 mJ) or the second harmonic (397 nm, 30 μJ) was employed. At least three photons at 794 nm or two photons at 397 nm are necessary to ionise *para*-xylylene. Both laser pulses enter the main chamber from the same side under a small angle and are softly focused on the interaction region with the molecular beam (266 nm: 700 mm lens, 794/397 nm: 500 mm lens), where the focal points are situated after the interaction region so as to minimise one-colour ionisation. The probe laser was delayed with respect to the pump laser using a computer-controlled stepper motor. The time intervals between the points varied between 17 fs, close to the pump–probe overlap, and up to 13 ps far away from it. Each delay trace consists of at least 6 individual delay scans. Mass spectra and photoelectron spectra were integrated over 150 laser shots for each point. The points during each scan were measured randomly. The polarisation of the pump laser was rotated for each point between parallel/perpendicular with respect to the probe laser, and no rotational anisotropy could be observed. Photoelectron spectra were calibrated using the one-colour ionisation in the $X^+\ ^2\Pi_g$ state of molecular oxygen with 266 nm radiation. Photoelectron images were inverted employing the pBasex algorithm[35] using even Legendre polynomials up to the 6^{th} order (P_6) to fit the angular distribution. A significant signal was only observed in the isotropic distribution (P_0) and in second order (P_2). The pump-only/probe-only signal was measured randomly for each series and subtracted from each point.

3 Computational methods

The electronic absorption spectrum of *para*-xylylene was calculated after determining the minimum energy structure of the electronic ground state employing different quantum chemical methods: The semiempirical configuration interaction method with single and double excitations (CISD)[36,37] using OM3[38,39] parametrisation with an active space of ten occupied and nine virtual orbitals employing the MNDO program,[40] as well as time-dependent density functional theory, using the long-range corrected functionals CAM-B3LYP[41] and ωB97XD[42] and the basis set aug-cc-pVTZ[43,44] within the Gaussian quantum chemical program package.[45] Furthermore, after structure optimization using the coupled cluster singles and doubles (CCSD) approach[46,47] with the cc-pVTZ basis set,[43] the excited states have been also calculated using the following wavefunction-based *ab initio* methods, employing the aug-cc-pVTZ basis set: algebraic diagrammatic construction to second order (ADC(2)),[48–50] using the Turbomole program package,[51] equation-of-motion (EOM)-CCSD[52,53] using the Gaussian program package, as well as multireference CISD (CAS-MRCISD)[54–56] and second-order perturbation theory (CAS-PT2)[57,58] using the Molpro package.[59] The orbitals for the CAS-MRCISD and CAS-PT2 calculations have been optimised separately for each symmetry species employing the complete active space self-consistent field method (CASSCF)[60,61] using an active space of 8 electrons in 11 orbitals.

The photodynamics of *para*-xylylene were simulated using our field-induced surface hopping methodology (FISH)[62] coupled to semiempirical CISD employing the OM3 parametrisation in the active space mentioned above. In the FISH approach, an electronic Schrödinger equation is solved along each classical trajectory in the manifold of several electronic states coupled by an electric field as well as nonadiabatic effects. For the coupling, electronic transition dipole moments as well as scalar nonadiabatic coupling elements are calculated along the trajectories. The electric field was taken to be a Gaussian-shaped pulse,

$$E(t) = E_0 \exp\left(-\frac{4 \ln 2}{a^2}(t - t_0)^2 \right) \cos(\omega(t - t_0)), \quad (1)$$

with $E_0 = 5.174 \times 10^{-3} \frac{E_h}{e a_0}$ (corresponding to 10^{12} W cm^{-2}), $\hbar\omega = 4.65$ eV, $a = 100$ fs and $t_0 = 200$ fs.

The 200 initial coordinates and momenta for the classical dynamics simulations were sampled from a harmonic Wigner distribution function at a temperature of 100 K. The nuclei were propagated by numerically solving Newton's equations of motion using the velocity Verlet algorithm[63] with a time step of 0.2 fs. The electronic degrees of freedom were propagated along the classical trajectories by solving the time-dependent Schrödinger equation in the manifold of the electronic ground and three excited states,[62] and the hopping probabilities were determined from the rate of change of the electronic populations.[64] The total photoion intensities were simulated by calculating the vertical ionisation energies from the actual electronic state along all FISH trajectories and summing up for each time step those trajectories where the energy of up to four photons of the experimental probe pulse was sufficient to ionise the molecule.

4 Results

4.1 Excited electronic states of *para*-xylylene

In view of the shortcomings and partially contradicting conclusions of previous theoretical investigations, as summarised in the introduction, we performed extensive calculations of the lowest-lying singlet states using a variety of *ab initio* and semiempirical methods. The resulting energies and oscillator strengths are presented in Table 1. In the first step, we employed the high-level MR-CI and CASPT2 methods in order to determine the possible states within the energy range relevant to the experimental conditions. In this way, we established the presence of several ππ* valence excited states as well as a set of s and p Rydberg states in the energy range below 6 eV. Due to symmetry selection rules, only the transitions to the B_{2u} ππ* state and the B_{1u} 3s Rydberg state are one-photon allowed, the latter exhibiting an about a thousand times weaker oscillator strength than the former. Therefore we attribute the experimentally observed absorption below 5 eV[7,65] to the bright B_{2u} state. The *ab initio* MR-CI and CASPT2 methods, however, seem to overestimate the energy of this state, presumably due to the restricted active space used and the absence of higher than double excitations in these methods. Better agreement with experiment is obtained employing several TDDFT methods as well as ADC(2) and EOM-CCSD using a singlet reference state. These methods, however, are for fundamental unable to describe the doubly excited $2A_g$ state, which is the lowest excited state in MR-CI and CASPT2. Such a state had been already predicted by Flynn and Michl as the lowest lying one using the PPP method[13] and has recently been confirmed by Nanda and Krylov[66] who found an energy of 3.72 eV at the triplet geometry, using the spin-flip variant of EOM-CCSD which is able to describe doubly-excited singlet states based on a triplet reference state.

Table 1 Vertical excitation energies in eV and oscillator strengths (in parentheses). For symmetry labeling according to the D_{2h} point group, the molecule is assumed to lie in the *xy* plane, with *y* denoting its longer axis

State	Character	OM3-CISD[a]	CAM-B3LYP[b]	ωB97XD[b]	ADC(2)[b,c]	EOM-CCSD[b,c]	MR-CISD + Q[b,c,d,e]	CAS-PT2[b,c,d]
$2A_g$ (S_1)	ππ* (doubly exc.)	4.10 (0.00)	—	—	—	—	4.89 (0.00)	4.81
$1B_{2u}$ (S_2)	ππ*	4.50 (0.88)	4.41 (0.86)	4.39 (0.84)	4.53 (1.01)	4.96 (1.00)	5.33 (0.27)	5.32
$1B_{1g}$ (S_3)	ππ*	4.76 (0.00)	4.95 (0.00)	4.93 (0.00)	5.02 (0.00)	5.24 (0.00)	5.12 (0.00)	5.10
$2B_{1g}$	ππ*	—	5.23 (0.00)	5.16 (0.00)	5.43 (0.00)	—	5.76 (0.00)	5.71
$1B_{1u}$	Ryd-s	—	5.21 (0.003)	5.41 (0.003)	5.32 (0.003)	5.41 (0.002)	5.32 (0.003)	5.35
$1B_{3g}$	Ryd-p_y	—	5.57 (0.00)	5.79 (0.00)	5.69 (0.00)	5.82 (0.00)	5.72 (0.00)	5.76
$1B_{2g}$	Ryd-p_x	—	5.59 (0.00)	5.78 (0.00)	5.73 (0.00)	5.83 (0.00)	5.75 (0.00)	5.79

[a] 20 electrons in 19 orbitals. [b] Aug-cc-pVTZ. [c] CCSD(cc-pVTZ) optimized structure. [d] 8 electrons in 11 orbitals. [e] Davidson correction, ref. 67.

In an attempt to find a compromise between the need to describe this state and the efficiency considerations necessary to perform multistate dynamics simulations, we also investigated the excited states in the frame of semiempirical methods. The best agreement both with higher-level calculations and experimental data was obtained by the multireference OM3-CISD method, which provides the relevant $\pi\pi^*$ states including the doubly excited $2A_g$ state. Due to the minimal basis set employed in semiempirical methods, these cannot describe Rydberg excitations. However, our *ab initio* results make it clear that the lowest-lying Rydberg states in *para*-xylylene are consistently situated above the bright B_{2u} state and should therefore play only a negligible role in the excited state dynamics induced by the experimental laser wavelength. This gave us confidence to use the computationally efficient semiempirical CISD approach to simulate the photodynamics of *para*-xylylene in the frame of our FISH method.

To provide a realistic comparison to the experimental findings, we have calculated the thermally broadened absorption spectrum for the ensemble of all 200 initial structures to be used in the dynamics simulation, as shown in Fig. 2. Clearly, our calculated spectrum (orange) reproduces the experimental spectrum by Marquardt *et al.*[65] very well, exhibiting a broad band between 4 and 5 eV centred around 4.4 eV.

4.2 Field-induced surface hopping simulations

The laser-induced photodynamics has been simulated in the manifold of the electronic ground and the three lowest-lying excited singlet states. Although for the structure of the ground state minimum only the S_2 state is optically bright whereas S_1 and S_3 are dark, the state ordering changes depending on the initial structure employed in the dynamics, such that for about half of the trajectories the S_3 state is the bright one, thus necessitating its inclusion in the dynamics (*cf.* the unconvolved stick spectrum for the initial ensemble presented in the ESI, Fig. S1†). For the photoexcitation, a 100 fs Gaussian laser pulse centred around an energy of 4.65 eV with an intensity of 10^{12} W cm^{-2}, corresponding to the experimental laser pulse parameters was used. The whole ensemble was propagated for 1 ps, with the laser pulse being centred at 200 fs.

The resulting electronic state populations are shown in Fig. 3. At the temporal centre of the pulse, an efficient population transfer into the second and third excited states can be seen. Subsequently the population switches rapidly to the

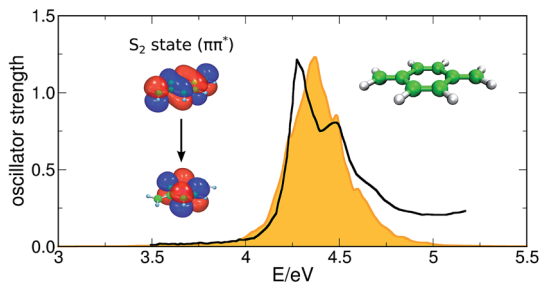

Fig. 2 Simulated thermally broadened absorption spectrum of *para*-xylylene (orange) and experimental data by Marquardt *et al.* (black).[65]

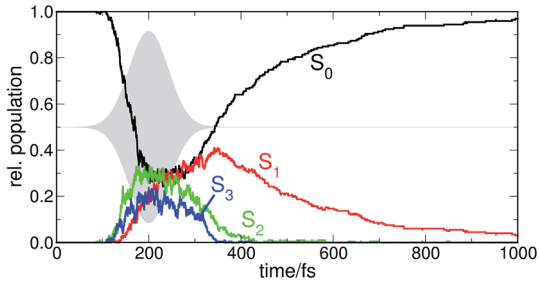

Fig. 3 Time-dependent electronic state populations of *para*-xylylene induced by a Gaussian laser pulse resonant to the $S_2 \leftarrow S_0$ transition. The pulse envelope is indicated in gray in the background and has a FWHM of 100 fs.

first excited state within ~100 fs, followed by a slow relaxation to the ground state within ~600 fs. After 1 ps almost all trajectories have returned to the ground state.

The deactivation mechanism leading back to the ground state noticeably often involves the passage through conical intersections (CIs). Between the first excited and the ground state, CIs were found at several accessible molecular geometries and are therefore determined to be one of the major pathways in the relaxation dynamics of *para*-xylylene (ESI, Fig. S2†). CIs were found at geometries with twisted methylene groups as well as boat conformations. Other trajectories show cyclisation, forming a cyclopropene structure. When analysing the relaxation of the whole ensemble, the trajectories can be categorised according to the geometry and the energy gap present at the final hops to the ground state (*cf.* ESI, Fig. S3†): After 325 fs, when the laser pulse is turned off, most hops occur at around 2.5 eV, and almost 1/4 of the trajectories deactivate through or close to CIs (energy gaps around 0 eV). More than 1/2 relax as a result of rotation or pyramidalisation of the methylene groups. Since these geometries are typical for potential CIs, this is accompanied by smaller values of the S_1–S_0 energy gaps at the final hops compared to trajectories that hop when the laser pulse is still present.

In Fig. 4a, the time-dependent state energies of an example trajectory together with molecular geometries at selected time steps are shown. The current state of the trajectory is indicated by the background colour. After excitation into the S_2 state, the molecule stays in this state for ~100 fs before changing to S_1. About 20 fs later, the molecule relaxes through a CI at a geometry with a twisted, pyramidalised methylene group (second geometry in Fig. 4, at 386 fs), resulting in a vibrationally hot ground state. This leads to a rotation of the terminal methylene groups with respect to the C6-ring plane as illustrated by the torsional angles presented in Fig. 4b. Fairly weak oscillation of the angles can be observed at the beginning of the trajectory. This changes with the excitation of the molecule, first leading to a twisted geometry at 300 fs where the second and first excited state cross, followed by the adoption of a second twisted geometry at 386 fs, at which the first excited state is depopulated through the CI mentioned above. A damped rotation/oscillation of the methylene group finally remains as a result of the increased internal vibrational energy.

In addition, a trajectory hopping at an energy gap of 2.5 eV is shown in the ESI, Fig. S4.† Compared to the trajectory shown in Fig. 4, it resides for a longer time in S_1, corresponding to the populations shown in Fig. 3. However, rotation and

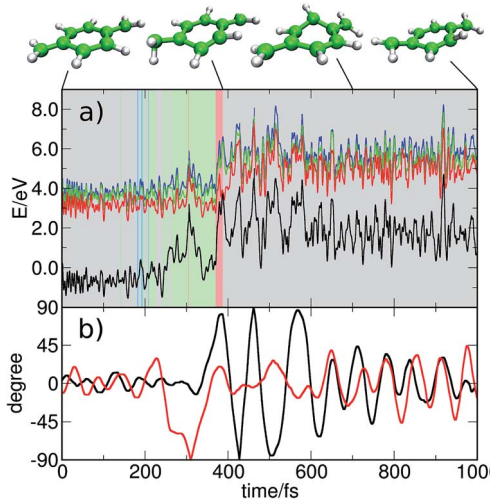

Fig. 4 (a) State energies of the ground (S_0, black) and lowest three excited states (S_1, red; S_2, green; S_3, blue) of an example trajectory. The background colours indicate the actual occupied state. Above, the molecular geometries at selected times are shown. (b) Torsional angle between each of the two methylene groups and the phenyl ring plane (black/red curves). The angle is measured between the line connecting the two methylene hydrogens and the average ring plane.

pyramidalisation also play a key role in the relaxation through this pathway, and the final hop to the ground state occurs on a comparable time scale.

Besides the structural changes accompanying the nonradiative relaxation process, another important issue we wish to address is the alteration of the system's biradicality in the course of the laser-induced dynamics. For this purpose, we calculated the natural orbital occupation numbers (NOONs) of the relevant orbitals of all states along the dynamics trajectories, which provide a quantitative measure for biradicality.[13,68] In Fig. 5, the NOONs of the four orbitals whose occupation numbers most strongly deviate from zero or two are shown along the trajectory presented in Fig. 4. We denote with HONO (highest occupied natural orbital)/HONO−1 the orbitals with initial occupation numbers close to two, and with LUNO (lowest unoccupied natural orbital)/LUNO+1 those with occupation numbers close to zero. The labeling as highest or lowest refers to the orbital's expectation value of the Fock operator (*cf.* ESI, Fig. S5†). Fig. 5 shows that initially the system has only marginal biradical character, which is evident from the NOONs of about 1.85 and 0.15 for the HONO and LUNO, respectively. Photoexcitation into the S_2 state is followed by a significant change of the NOONs at ∼150 fs and from 200 fs onwards, with the HONO and LUNO reaching values close to one. After reaching the S_1–S_0–CI at ∼385 fs, an immediate drop in biradicality is observed, followed by a significant fluctuation of the NOONs within the next 300 fs due to increased kinetic energy and thus pronounced geometry change of the trajectory. Comparison with the angles presented in Fig. 4b makes clear that in the electronic ground state strong oscillation of the biradical character is accompanied by large rotation of the methylene groups out of the molecular plane, while in the excited state the molecule is already biradical at

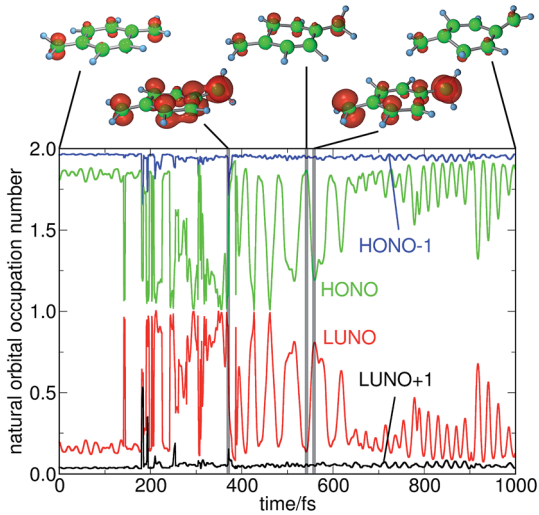

Fig. 5 Time-dependent natural orbital occupation numbers (NOONs) along the trajectory shown in Fig. 4; (upper part) surface plot of the unpaired electron density $U(\mathbf{r})$ at selected time steps.

planar geometries. A more detailed insight into the time-dependence of the biradical character can be obtained by introducing a spatial measure such as the unpaired electron density as proposed by Head-Gordon[69] which is defined as

$$U(\mathbf{r}) = \sum_i (1 - \mathrm{abs}(1 - n_i))|\psi_i(\mathbf{r})|^2 \quad (2)$$

with the electronic coordinates $\mathbf{r}$, the natural orbital $\psi_i(\mathbf{r})$ and the NOON of the orbital i, n_i. The surface plots of $U(\mathbf{r})$ depicted for selected time steps in the upper part of Fig. 5 show that a large magnitude of $U(\mathbf{r})$ correlates with NOONs close to one. By contrast, if all NOONs are either close to two or zero, this corresponds to small values of $U(\mathbf{r})$. While the system is electronically excited, $U(\mathbf{r})$ is delocalised over the whole molecule (Fig. 5, structure at 386 fs). In the electronic ground state, however, a localisation of the biradical character at the methylene carbon atoms is observed (Fig. 5, structure at 555 fs). Our analysis confirms the absence of biradicality in the thermal equilibrium of the ground state of *para*-xylylene. Nonetheless, after photoexcitation the system can be transiently regarded as a biradical within the time scale of vibronic relaxation.

To quantify the effective decay time of the biradical character of the whole ensemble, we present in Fig. 6 the NOONs of the four relevant orbitals averaged over all trajectories as a function of time. It can be seen that, as the pulse intensity increases, the NOONs also change transiently due to electronic excitation, leading to an overall increase of the biradical character. Subsequently the biradicality decays such that after about 1 ps, when almost all trajectories have returned to the ground state, the biradical character is largely lost again. Nevertheless, the NOONs of the HONO and LUNO still differ substantially from their values before excitation. This is due to the increased kinetic energy of the relaxed molecule, enabling the methylene groups of most of the trajectories to overcome the rotational barrier and therefore reach CIs, leading to an increased residual biradicality.

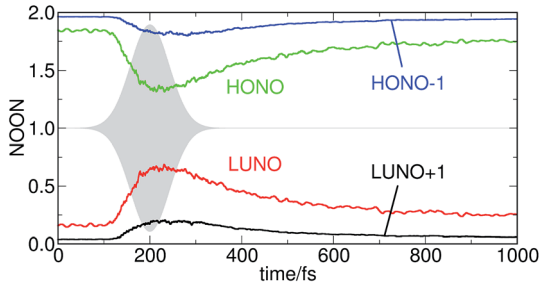

Fig. 6 Natural orbital occupation numbers (NOONs) averaged over all trajectories at each time step. In grey: laser pulse.

4.3 Time-resolved pump–probe experiments and simulations

Our simulations of the *para*-xylylene photodynamics are complemented by time- and angle-resolved pump–probe ionisation experiments. For this purpose, *para*-xylylene is generated *via* pyrolysis of its precursor [2.2]paracyclophane as described in the Experimental section. Mass spectra at pump–probe (266/794 nm) conditions prove the absence of any ionisable species before pyrolysis as well as the pyrolytic formation of *para*-xylylene ($m/z = 104$ signal, see ESI, Fig. S6†), which dominates the spectrum. Two other masses, $m/z = 78$, tentatively identified as the benzene cation, and $m/z = 103$, corresponding to the loss of one hydrogen atom, are observed, which show significantly lower intensity than the $m/z = 104$ peak (6% and 7% for $m/z = 78$ and 103, respectively). The additional peak at $m/z = 105$ is attributed to the ^{13}C satellite of $m/z = 104$. The peak width of $m/z = 103$ and especially of $m/z = 78$ is considerably larger than that of $m/z = 105$ (see ESI, Fig. S7†), indicating that these peaks are formed by dissociative photoionisation, probably from *para*-xylylene itself. The time-resolved data discussed below originate therefore from *para*-xylylene. At 397 nm probe wavelength, the relative intensity of the side masses $m/z = 78$ and 103 increases slightly (see ESI, Fig. S8†), but the mass spectrum remains dominated by the signal of the molecular ion.

Based on the computed absorption spectrum (*cf.* Fig. 2 and Table 1), excitation of *para*-xylylene at 266 nm populates the optically bright B_{2u} state (S_2/S_3). In Fig. 7 (upper trace), the temporal intensity evolution after 266 nm excitation of the masses $m/z = 104$ (*para*-xylylene, black circles), 103 (red diamonds) and 78 (blue triangles) normalised to the respective intensity maximum are displayed. Interestingly, the maxima of the $m/z = 78$ and 103 intensities are delayed by about 70 fs with respect to that of the $m/z = 104$ signal (see Fig. 7, upper inset). In principle, these side masses could correspond to independent pyrolysis products. In this case, only very slight differences due to different ionisation schemes ([1 + 3′] *vs.* [1 + 4′]) leading to different instrument response functions (IRF) are expected. A 70 fs shift is significant and larger than the shift expected from the instrument response function. Furthermore, as mentioned above, the translational energy distribution extracted from the ion images suggest that both peaks are due to fragmentation (see ESI, Fig. S7†). Therefore, the side masses are not independent pyrolysis products, but fragments of *para*-xylylene ($m/z = 104$) issued from photodissociative ionisation. In agreement with the computations discussed above we propose a sequential mechanism:

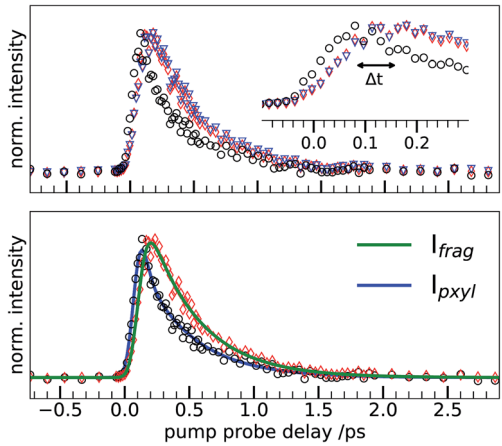

Fig. 7 Normalised decays at 794 nm probe wavelength of mass spectra signals $m/z = 104$ (*para*-xylylene, black circles), 103 (red diamonds) and 78 (blue triangles). The upper part shows the experimental decays of all three mass spectra signals, and the time shift between $m/z = 104$ and 103/78 is clearly visible in the inset. In the lower part, $m/z = 104$ and 103 are fitted according to eqn (4) and (5), respectively, with $\tau_1 = 40 \pm 7$ fs, $\tau_2 = 393 \pm 39$ fs and IRF $= 114 \pm 7$ fs. Similar fit constants are obtained when fitting $m/z = 104$ and $m/z = 78$ according to these equations.

$$S_2 \xrightarrow{\tau_1} S_1 \xrightarrow{\tau_2} \text{dark} \tag{3}$$

Initially excited *para*-xylylene decays from the state S_2 with a first time constant τ_1 to the S_1 state. Here the masses $m/z = 78$ and 103 are created only after this first relaxation of *para*-xylylene. The S_1 state then decays to the ground state which can no longer be ionised. Setting up a kinetic model for this proposed sequential mechanism leads to the following expression for the observable time-dependent signal of the *para*-xylylene $I_{\text{pxyl}}(t)$ and of its fragments $I_{\text{frag}}(t)$:

$$I_{\text{pxyl}}(t) = \left\{ \sigma_1 e^{-\frac{t}{\tau_1}} + \sigma_2 \frac{\tau_2}{\tau_1 - \tau_2} \left(e^{-\frac{t}{\tau_1}} - e^{-\frac{t}{\tau_2}} \right) \right\} * e^{-\frac{t^2 \ln 2}{\text{IRF}^2}} \tag{4}$$

$$I_{\text{frag}}(t) = \left\{ \sigma_3 \frac{\tau_2}{\tau_1 - \tau_2} \left(e^{-\frac{t}{\tau_1}} - e^{-\frac{t}{\tau_2}} \right) \right\} * e^{-\frac{t^2 \ln 2}{\text{IRF}^2}} \tag{5}$$

where σ_1, σ_2 and σ_3 are cross sections, and * symbolises the convolution operator. The time constants τ_1 and τ_2 need to satisfy both equations, therefore the *para*-xylylene and the fragment data are fitted simultaneously. For the case of masses 104 and 103, this leads to the fit curves yielding time constants of $\tau_1 = 40 \pm 7$ fs, $\tau_2 = 393 \pm 9$ fs, as presented in the lower part of Fig. 7. The time constants for the two steps agree well with the results of the dynamics calculations described above. Nearly identical results are obtained for a simultaneous fit of $m/z = 104$ and 78. The first very short time constant $\tau_1 = 40$ fs compared to the IRF of 114 ± 7 fs is indeed only justifiable because it is reflected in the delayed onset of the fragment signals. This hints at a mechanism in which the probe step leads to different states of the ion, depending on whether the ionisation proceeds from the S_1 or the

S_2 state.[70] The appearance of the fragment signal might also be attributed to the increased vibrational energy of the parent ion when ionised from the S_1 state. With 397 nm as the probe wavelength the observation is similar, although the decays are noisier and the time shift less pronounced (see ESI, Fig. S9†).

Since the mass spectra are dominated by the *para*-xylylene signal, time-resolved photoelectron spectra (TRPES) were recorded as well, which should provide additional information on the photodynamics of *para*-xylylene. The TRPES obtained with 794 nm probe wavelength is displayed in Fig. 8. In the left panel, the photoelectron spectrum integrated over all delay times is presented, where the maximum kinetic energies of the electrons (eKe) possible for a given multi-photon process $[1 + m']$ are indicated as blue lines. At least 3 probe photons are required to surpass the ionisation limit; a signal arising from a $[1 + 4']$ process is also observed. With three probe photons ($E_{\mathrm{pump+3\times probe}} = 9.32$ eV) only the D_0 $X^+\ ^2B_{3u}$ state is energetically accessible ($eKe_{max} = 1.5$ eV). With four probe photons, however, the D_1-state ($IE(A^+\ ^2B_{1g}) = 9.7$ eV)[21] can also be reached ($eKe_{max} = 1.2$ eV) in addition to four-photon ionisation to D_0 ($eKe_{max} = 3.0$ eV). The photoelectron spectrum shows a broad band with four identifiable peaks at 0.14, 0.55, 1.01 and 1.25 eV, which could stem from ionisation to both the D_0- or D_1-states. These four peaks do not correspond to vibrations in the cation as measured recently in the threshold photoelectron spectrum.[22] Assuming ionisation into the D_0-state, the three higher-energetic peaks could be tentatively assigned to ionising from an intermediate p-Rydberg series with the last 794 nm photon, but the peak at 0.14 eV remains unassigned. The presence of intermediate Rydberg states in the ionisation process leads to characteristic resonances as has been observed before,[24,71–73] but in such a case a change in the photoelectron spectrum upon varying the probe wavelength is expected. The main features of the TRPES with 397 nm probe (see ESI, Fig. S10†), however, are similar to the TRPES with 794 nm, although only ionisation by a $[1 + 2']$-process is

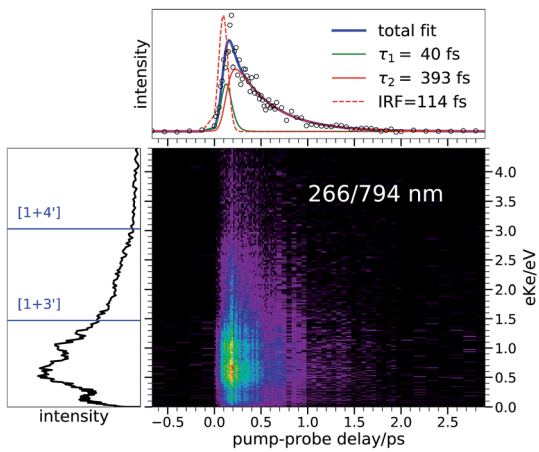

Fig. 8 TRPES with 266 nm pump/794 nm probe. The time dependence of the total photoelectron signal (top trace) can be fitted with a biexponential decay ($\tau_1 = 40$ fs, $\tau_2 = 393$ fs, IRF = 114 fs), where the time constants and the IRF were provided from the fit of the ion decays presented in Fig. 7. The graph on the left shows the photoelectron kinetic energy summed over all delay times.

possible. The photoelectron spectrum is broad, exhibiting four peaks at similar positions as in the 794 nm probe TRPES (0.18, 0.52, 1.00 and 1.58 eV). Selected traces of the photoelectron spectra at different delay times are displayed in Fig. 9. At early times only [1 + 3′] ionisation is observed, whereas at later times [1 + 4′] ionisation grows in relative intensity. It is tempting to discuss this observation within Koopmans' type photoionisation correlations, where different excited electronic states correlate with different electronic states of the ion as reported by Blanchet *et al.* for the decatetratene molecule.[70] The bright S_2 state is dominated by a HOMO → LUMO transition and is correlated upon one-photon ionisation (removal of an electron from the LUMO) with the D_0 state of the cation. The dark S_1 state on the other hand is a doubly excited state and upon ionisation correlates to the D_1 state of the cation, because one electron remains in the LUMO. However, the multiphoton nature of the probe step does not permit such a simple interpretation, since the correlations can be modified by intermediate resonances. In fact, the observation of electrons with comparably high kinetic energy above 1.5 eV at long delay times suggests a correlation between S_1 and D_0 at least for four-photon ionisation. At short delay times the photoelectron signal maximises at low kinetic energies. Such low-energy electrons appear to be correlated with the photoionisation of S_2 to D_0 by three photons or to D_1 in a four-photon process.

The D_0 *para*-xylylene cations formed by ionisation from S_1 possess considerable internal energy, and part of them will fragment, leading to the delayed onset of $m/z = 103$ and 78 as observed in the time-resolved mass spectra. Since the photoelectron bands corresponding to S_2 and S_1 overlap, a deconvolution of the photoelectron spectra is difficult. The total photoelectron decay (Fig. 8, upper panel), however, is in perfect agreement (time constants $\tau_1 = 40$ fs, $\tau_2 = 393$ fs) with the ion signal decay. The observed photoelectron anisotropy β_2 was positive with values between 0.8 and 1.2 for the whole photoelectron spectrum and did not change over time. As the interpretation of photoelectron anisotropies for multiphoton ionisation processes is very intricate, and unlikely to provide unambiguous information, these values will not be further discussed.

To establish a direct connection between our dynamics simulations and the experimental time-resolved signals, the total photoionisation intensities were simulated as well. For this purpose, we calculated the vertical ionisation energies from the actual electronic state to the cationic D_0 and D_1 states along all surface hopping trajectories, and considered the ionisation possible when the ionisation energy was surpassed by the experimental probe photon energy. Although in the experiment ionisation is achieved by up to four 794 nm photons (4 × 1.56 eV) while the theoretical values correspond to one-photon ionisation at 266 nm (1 ×

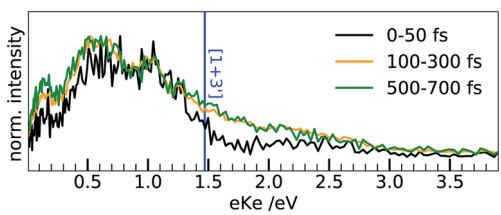

Fig. 9 Selected traces of the TRPES with 266 nm pump/794 nm probe for different delay time intervals (*cf.* Fig. 8). Each trace is normalised on its maximum.

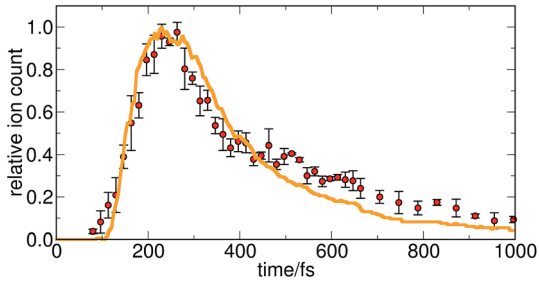

Fig. 10 Simulated time-resolved ion intensities (orange) based on the FISH simulation presented in Fig. 3, employing a probe energy of 6.24 eV (4 × 794 nm), and experimental ion intensities for 266 nm excitation and 794 nm ionisation (red dots and error bars).

6.24 eV), the results are comparable since the signals largely depend only on the energetic accessibility of the ionic states. In Fig. 10, the simulated total energy-integrated, time-dependent ionisation intensities (orange) and the experimental values are presented. Both signals are in very good agreement with each other, revealing a biexponential decay, which is assigned to the relaxation from the initially populated higher states into the S_1 state followed by the slower return from the S_1 to the S_0 ground state, as evident from the dynamics simulations. An intensity loss of about 50% is observed within 100 fs after reaching the intensity maximum, and within the following 600 fs, the signal drops to about 10%. These findings are consistent with the assumed sequential decay mechanism, which was also deduced from the experimental data.

5 Conclusions

We elucidated the ultrafast photodynamics of *para*-xylylene after optical excitation at 266 nm in a joint experimental and computational study. Using field-induced surface hopping we simulated the excited-state dynamics of *para*-xylylene after excitation in the optically bright S_2-state, revealing a sequential decay *via* the S_1 back to the ground state. This mechanism was confirmed by both time-resolved mass spectrometry and photoelectron spectroscopy. While the molecular ion signal decays biexponentially with time constants of $\tau_1 = 40$ fs and $\tau_2 = 393$ fs, fragment ion signals grow with a rise time corresponding to τ_1 and decay with time constant τ_2. While ionisation from S_2 only forms the molecular ion, ionisation from S_1 leads to partial dissociative photoionisation. At late delay times a contribution at high kinetic energies to the photoelectron signal is recognisable. This can be qualitatively understood when different probabilities for ionisation into D_0 and D_1 are taken into account. The characteristic signatures of both S_2 and S_1 ionisation permit to disentangle quantitatively and qualitatively the two deactivation steps in the mass spectra and photoelectron spectra. An excellent agreement between the observed and the simulated ion signal is obtained.

Conflicts of interest

There are no conflicts to declare.

Acknowledgements

The authors kindly thank Olivier Gobert, Michel Perdrix and Delphine Guillaumet for setting up and maintaining the SLIC/LUCA laser. This work was supported by the Deutsche Forschungsgemeinschaft, Research Training School, GRK 2112 "Molecular Biradicals: Structure, Properties and Reactivity". KI, AR and JP thank COST action CM1405 MOLIM for support. LP and IF acknowledge funding by DAAD and Campus France, PHC PROCOPE 32980XH. Finally, LP acknowledges ANR11-EQPX0005-ATTOLAB for support.

References

1 M. Szwarc, *J. Chem. Phys.*, 1948, **16**, 128–136.
2 P. Dagaut, G. Pengloan and A. Ristori, *Phys. Chem. Chem. Phys.*, 2002, **4**, 1846–1854.
3 M. Shapero, N. Cole-Filipiak, C. Haibach-Morris and D. M. Neumark, *J. Phys. Chem. A*, 2015, **119**, 12349–12356.
4 G. da Silva, J. Cole and J. Bozzelli, *J. Phys. Chem. A*, 2009, **113**, 6111–6120.
5 American Society for Testing Materials and American Petroleum Institute, Research Project 45, Knocking Characteristics of Pure Hydrocarbons: Developed Under American Petroleum Institute Research Project 45, 1958.
6 M. Szwarc, *Discuss. Faraday Soc.*, 1947, **2**, 46–49.
7 J. R. Schaefgen, *J. Polym. Sci.*, 1955, **15**, 203–219.
8 L. A. Errede and M. Szwarc, *Q. Rev. Chem. Soc.*, 1958, **12**, 301–320.
9 W. F. Gorham, *J. Polym. Sci., Part A-1*, 1966, **4**, 3027–3039.
10 W. S. Trahanovsky and S. P. Lorimor, *J. Org. Chem.*, 2006, **71**, 1784–1794.
11 K. Pachner, M. Steglich, P. Hemberger and I. Fischer, *J. Chem. Phys.*, 2017, **147**, 084303.
12 C. A. Coulson, D. P. Craig, A. Maccoll and A. Pullman, *Discuss. Faraday Soc.*, 1947, **2**, 36–38.
13 C. R. Flynn and J. Michl, *J. Am. Chem. Soc.*, 1974, **96**, 3280.
14 P. C. Hiberty and P. Karafiloglou, *Theor. Chim. Acta*, 1982, **61**, 171–177.
15 D. J. Williams, J. M. Pearson and M. Levy, *J. Am. Chem. Soc.*, 1970, **92**, 1436.
16 J. M. Pearson, H. A. Six, D. J. Williams and M. Levy, *J. Am. Chem. Soc.*, 1971, **93**, 5034–5036.
17 P. G. Mahaffy, J. D. Wieser and L. K. Montgomery, *J. Am. Chem. Soc.*, 1977, **99**, 4514–4515.
18 T.-K. Ha, *Theor. Chim. Acta*, 1984, **66**, 111–120.
19 M. Bobrowski, P. Skurski and S. Freza, *Chem. Phys.*, 2011, **382**, 20–26.
20 Due to differently chosen coordinate axes, the state has B_{1u} symmetry in this publication.
21 T. Koenig, R. Wielesek, W. Snell and T. Balle, *J. Am. Chem. Soc.*, 1975, **97**, 3225–3226.
22 P. Hemberger, A. J. Trevitt, E. Ross and G. D. Silva, *J. Phys. Chem. Lett.*, 2013, **4**, 2546–2550.
23 M. J. S. Dewar, *J. Am. Chem. Soc.*, 1982, **104**, 1447–1449.
24 A. Röder, K. Issler, L. Poisson, A. Humeniuk, M. Wohlgemuth, M. Comte, F. Lepetit, I. Fischer, R. Mitrić and J. Petersen, *J. Chem. Phys.*, 2017, **147**, 013902.

25 A. Röder, A. Humeniuk, J. Giegerich, I. Fischer, L. Poisson and R. Mitrić, *Phys. Chem. Chem. Phys.*, 2017, **19**, 12365–12374.
26 T. Fuji, Y. I. Suzuki, T. Horio, T. Suzuki, R. Mitrić, U. Werner and V. Bonačić-Koutecký, *J. Chem. Phys.*, 2010, **133**, 234303.
27 J. Stanzel, M. Neeb, W. Eberhardt, P. G. Lisinetskaya, J. Petersen and R. Mitrić, *Phys. Rev. A: At., Mol., Opt. Phys.*, 2012, **85**, 013201.
28 A. Humeniuk, M. Wohlgemuth, R. Suzuki and T. Mitrić, *J. Chem. Phys.*, 2013, **139**, 134104.
29 J. Giegerich, J. Petersen, R. Mitrić and I. Fischer, *Phys. Chem. Chem. Phys.*, 2014, **16**, 6294–6302.
30 Y. Yamamoto, Y. I. Suzuki, G. Tomasello, T. Horio, S. Karashima, R. Mitrić and T. Suzuki, *Phys. Rev. Lett.*, 2014, **112**, 187603.
31 P. G. Lisinetskaya, C. Braun, S. Proch, Y. D. Kim, G. Ganteför and R. Mitrić, *Phys. Chem. Chem. Phys.*, 2016, **18**, 6411–6419.
32 D. W. Kohn, H. Clauberg and P. Chen, *Rev. Sci. Instrum.*, 1992, **63**, 4003–4005.
33 A. T. J. B. Eppink and D. H. Parker, *Rev. Sci. Instrum.*, 1997, **68**, 3477–3484.
34 E. Gloaguen, J. M. Mestdagh, L. Poisson, F. Lepetit, J. P. Visticot, B. Soep, M. Coroiu, A. T. J. B. Eppink and D. H. Parker, *J. Am. Chem. Soc.*, 2005, **127**, 16529–16634.
35 G. A. Garcia, L. Nahon and I. Powis, *Rev. Sci. Instrum.*, 2004, **75**, 4989–4996.
36 A. Koslowski, M. E. Beck and W. Thiel, *J. Comput. Chem.*, 2003, **24**, 714–726.
37 S. Patchkovskii, A. Koslowski and W. Thiel, *Theor. Chem. Acc.*, 2005, **114**, 84–89.
38 M. Scholten, Ph.D. thesis, Universität Düsseldorf, Germany, 2003.
39 W. Weber and W. Thiel, *Theor. Chem. Acc.*, 2000, **103**, 495.
40 W. Thiel, *MNDO program*, Max-Planck-Institut für Kohlenforschung, Mühlheim, Germany, 2007.
41 T. Yanai, D. P. Tew and N. C. Handy, *Chem. Phys. Lett.*, 2004, **393**, 51–57.
42 J.-D. Chai and M. Head-Gordon, *Phys. Chem. Chem. Phys.*, 2008, **10**, 6615–6620.
43 T. H. Dunning Jr, *J. Chem. Phys.*, 1989, **90**, 1007.
44 R. A. Kendall, T. H. Dunning Jr and R. J. Harrison, *J. Chem. Phys.*, 1992, **96**, 6796.
45 M. J. Frisch, G. W. Trucks, H. B. Schlegel, G. E. Scuseria, M. A. Robb, J. R. Cheeseman, G. Scalmani, V. Barone, B. Mennucci, G. A. Petersson, H. H. Nakatsuji, M. Caricato, X. Li, H. P. Hratchian, A. F. Izmaylov, J. Bloino, G. Zheng, J. L. Sonnenberg, M. Hada, M. Ehara, K. Toyota, R. Fukuda, J. Hasegawa, M. Ishida, T. Nakajima, Y. Honda, O. Kitao, H. Nakai, T. Vreven, J. A. Montgomery Jr, J. E. Peralta, F. Ogliaro, M. Bearpark, J. J. Heyd, E. Brothers, K. N. Kudin, V. N. Staroverov, R. Kobayashi, J. Normand, K. Raghavachari, A. Rendell, J. C. Burant, S. Iyengar, J. S. Tomasi, M. Cossi, N. Rega, J. M. Millam, M. Klene, J. E. Knox, J. B. Cross, V. Bakken, C. Adamo, J. Jaramillo, R. Gomperts, R. E. Stratmann, O. Yazyev, A. J. Austin, R. Cammi, C. Pomelli, J. W. Ochterski, R. L. Martin, K. Morokuma, V. G. Zakrzewski, G. A. Voth, P. Salvador, J. J. Dannenberg, S. Dapprich, A. D. Daniels, O. Farkas, J. B. Foresman, J. V. Ortiz, J. Cioslowski and D. J. Fox, *Gaussian 09, Revision D01, Gaussian, Inc.*, 2009.
46 G. D. Purvis III and R. J. Bartlett, *J. Chem. Phys.*, 1982, **76**, 1910.
47 G. E. Scuseria, C. L. Janssen and H. F. Schaefer III, *J. Chem. Phys.*, 1988, **89**, 7382.

48 J. Schirmer, *Phys. Rev. A: At., Mol., Opt. Phys.*, 1982, **26**, 2395.
49 A. B. Trofimov and J. Schirmer, *J. Phys. B: At., Mol. Opt. Phys.*, 1995, **28**, 2299.
50 C. Hättig, *Adv. Quantum Chem.*, 2005, **50**, 37.
51 TURBOMOLE V7.0 2015, *A Development of University of Karlsruhe and Forschungszentrum*, Karlsruhe GmbH, available from http://www.turbomole.com.
52 H. Koch and P. Jorgensen, *J. Chem. Phys.*, 1990, **93**, 3333.
53 J. F. Stanton and R. J. Bartlett, *J. Chem. Phys.*, 1993, **98**, 7029.
54 P. J. Knowles and H. J. Werner, *Chem. Phys. Lett.*, 1988, **145**, 514.
55 P. J. Knowles and H. J. Werner, *Theor. Chim. Acta*, 1992, **84**, 95.
56 H. J. Werner and P. J. Knowles, *J. Chem. Phys.*, 1988, **89**, 5803.
57 K. Andersson, P.-Å. Malmqvist, B. Roos, A. Sadlej and K. Wolinski, *J. Phys. Chem.*, 1990, **94**, 5483.
58 K. Andersson, P.-Å. Malmqvist and B. Roos, *J. Chem. Phys.*, 1992, **96**, 1218.
59 H.-J. Werner, P. J. Knowles, G. Knizia, F. R. Manby and M. Schütz, *MOLPRO, Version 2015.1, a Package of Ab Initio Programs*, 2015, see http://www.molpro.net.
60 P. J. Knowles and H. J. Werner, *Chem. Phys. Lett.*, 1985, **115**, 259.
61 H. J. Werner and P. J. Knowles, *J. Chem. Phys.*, 1985, **82**, 5053.
62 R. Mitrić, J. Petersen and V. Bonačić-Koutecký, *Phys. Rev. A: At., Mol., Opt. Phys.*, 2009, **79**, 053416.
63 L. Verlet, *Phys. Rev.*, 1967, **159**, 98.
64 R. Mitric, J. Petersen and V. Bonacic-Koutecký, Multistate Nonadiabatic Dynamics 'on the Fly' in Complex Systems and Its Control by Laser Fields, in *Conical Intersections: Theory, Computation and Experiment*, ed. W. Domcke, D. R. Yarkony and H. Köppel, World Scientific, Singapore, 2011, vol. 17, pp. 497–568, (Advanced Series in Physical Chemistry).
65 R. Marquardt, W. Sander, T. Laue and H. Hopf, *Liebigs Ann.*, 1995, 1643.
66 K. D. Nanda and A. I. Krylov, *J. Chem. Phys.*, 2017, **146**, 224103.
67 E. R. Davidson and D. W. Silver, *Chem. Phys. Lett.*, 1977, **52**, 403–406.
68 D. Döhnert and J. Koutecký, *J. Am. Chem. Soc.*, 1980, **102**, 1789–1796.
69 M. Head-Gordon, *Chem. Phys. Lett.*, 2003, **372**, 508–511.
70 V. Blanchet, M. Z. Zgierski, T. Seideman and A. Stolow, *Nature*, 1999, **401**, 52–54.
71 M. Tsubouchi and T. Suzuki, *J. Phys. Chem. A*, 2003, **107**, 10897.
72 J. Gosselin and P. Weber, *J. Phys. Chem. A*, 2005, **109**, 4899–4904.
73 P. Hemberger, J. Köhler, I. Fischer, G. Piani, L. Poisson and J.-M. Mestdagh, *Phys. Chem. Chem. Phys.*, 2012, **14**, 6173–6178.

